

**TABLE 1 Performance Comparison Between the Present work and the Recently Published Ones**

Initial $C_0$ (pF)	0.046	1.0	0.108	0.8	0.37	0.28
$Q$ (@2 GHz)	40	5	20	133	35	46
Tuning range (%)	55.6	100	203	24	192	210
Self-resonant freq. (GHz)	>10	4.8	>3	>5	8.25	9.44
Max. driving voltage	17	3.2	6	20	4	4
Tuning method	gap	area	gap and area	gap	gap	area
Substrate	glass	SOI	CMOS silicon	alumina	CMOS silicon	CMOS silicon
References	[3]	[4]	[5]	[7]		This work

ing from the series parasitic inductance and resistance of the fold-beams that is used for actuation. An optimized spring structure is under consideration to replace in future to improve the RF performance at high frequency. Moreover, larger initial capacitance values could be achieved by further increasing the thickness of the metal structure.

#### 4. CONCLUSION

Both area-tuning and gap-tuning types of low-voltage wide-tuning variable capacitors are formed by using a novel low-cost metal micromachining technique. With only two layers of mask used, the post-CMOS compatible micromachining process is with a potential to integrate the RF passives into RF ICs. The fabricated area-tuning and gap-tuning capacitors have demonstrated large tuning ratios of 3.1:1 and 2.92:1, respectively, under a low actuating voltage of 4 V. High  $Q$ -factor of 169 at 1 GHz and 46 at 2 GHz for the area-tuning capacitor, as well as, 87 at 1 GHz and 35 at 2 GHz for the gap-tuning capacitor are measured. In view of the large tuning range and the high RF performance, these variable capacitors are promising as building blocks for on-chip RF applications. Besides, the developed metal micromachining technique can be widely used for post-CMOS integration of the RF passives with RF ICs.

#### ACKNOWLEDGMENT

This work is supported by the Chinese 973 Program (2006CB300405). The authors thank Prof. Xiaowei Sun, Prof. Yuelin Wang, and Ms. Rong Qian for their helps in the  $S$ -parameters test and academic discussions.

#### REFERENCES

1. C.Y. Nguyen, L.P.B. Katehi, and G.M. Rebeiz, Micromachined devices for wireless communications Proc IEEE 86 (1998), 1756–1768.
2. D.J. Young, V. Malba, J.J. Ou, A.F. Bemhardt, and B.E. Boser, A micromachined variable capacitor for monolithic low-noise VCOs, Tech Digest Solid State Sensor and Actuator Workshop, June 1988, pp. 128–131.
3. J. Chen, J. Zou, C. Liu, J.S. Aine, and S. Kang, Design and modeling of a micromachined high- $Q$  tunable capacitor with large tuning range and a vertical planar spiral inductor, IEEE Trans Electron Dev 50 (2003), 730–739.
4. A.D. Yalcinkaya, S. Jensen, and O. Hansen, Low voltage, high- $Q$  SOI MEMS varactors for RF applications, IEEE Solid-State Circuits Conf ESSCIRC'03, September 2003, pp. 607–610.
5. A. Oz and G.K. Fedder, CMOS-compatible RF MEMS tunable capacitors, IEEE Microwave Symp Dig, Philadelphia, PA (2003), A97–A100.
6. J.J. Yao, RF MEMS from a device perspective, J Micromech Microeng 10 (2000), R9–R38.
7. D.M. Klymyshyn, D.T. Haluzan, M. Borner, S. Achenbach, J. Mohr, and T. Mappes, High aspect ratio vertical cantilever RF-MEMS variable capacitor, IEEE Microwave Wireless Compon Lett 17 (2007), 127–129.
8. L.S. Stephens, K.W. Kelly, S. Simhadri, A.B. McCandless, and E.I.

Meletis, Mechanical property evaluation and failure analysis of cantilevered LIGA nickel Microposts, IEEE J Microelectromech Syst 10 (2001), 347–359.

9. L. Gu and X.X. Li, Concave-suspended high- $Q$  solenoid inductors with an RFIC-compatible bulk-micromachining technology, IEEE Trans Electron Dev 54 (2007), 882–885.
10. L. Gu and X.X. Li, A post-CMOS concave-suspending MEMS process in standard silicon wafers for high-performance solenoidal-DNA-configured micro-transformers, IEEE International Electron Devices Meeting (IEDM'06), December 2006, pp. 521–524.
11. M. Bao, Micro mechanical transducer, In: S. Middelhoek (Ed.), Handbook of sensors and actuators, Vol. 8, Elsevier, Amsterdam, 2000.

© 2008 Wiley Periodicals, Inc.

## SIMULTANEOUS MEASUREMENT OF TEMPERATURE AND STRAIN BASED ON ARC-INDUCED LONG-PERIOD FIBER GRATINGS. A CASE STUDY

G. Rego<sup>1,2</sup>

<sup>1</sup> UOSE, INESC-Porto, R. Campo Alegre 687, 4169–007 Porto, Portugal

<sup>2</sup> Escola Superior de Tecnologia e Gestão-IPVC, 4900–348 Viana do Castelo, Portugal; Corresponding author: gmrego@fc.up.pt

Received 7 January 2008

**ABSTRACT:** We present a potential sensor head for the simultaneous measurement of temperature and strain based on the concatenation of two long-period fiber gratings arc-induced in different fibers. Despite being the temperature and strain sensitivities of the individual gratings well defined, we demonstrate that the sensor cannot perform the simultaneous measurement of those physical parameters. This fact, results from the uncertainty in finding the determinant of the inverse matrix. © 2008 Wiley Periodicals, Inc. Microwave Opt Technol Lett 50: 2472–2474, 2008; Published online in Wiley InterScience (www.interscience.wiley.com). DOI 10.1002/mop.23644

**Key words:** temperature and strain measurement; optical sensing; long-period fiber gratings; arc-induced gratings

### 1. INTRODUCTION

Long-period fiber gratings (LPGs) have been used as sensing elements for simultaneous measurements of temperature and strain [1–4]. In general, the ability to discriminate between two or more parameters is based on the different responses shown by two particular resonances belonging to two concatenated gratings. Recently, it was demonstrated that the response of arc-induced gratings to strain and temperature could be controlled by changing gratings fabrication parameters [5]. By employing the properties of those gratings, a sensor head consisting of two concatenated LPGs with cladding mode stripping in between was implemented

for temperature and strain measurements. An index matching gel was applied to the fiber to strip cladding modes to eliminate recoupling in the second grating. Unfortunately, the use of gel strongly limits the range of working temperature. A possibility to extend the working range is to recoat the fiber in the region between the two gratings.

In this article we discuss the performance of a sensor head consisting of two concatenated gratings arc-induced in two different fibers.

## 2. EXPERIMENTAL RESULTS AND DISCUSSION

To implement the sensor, two steps were performed. First, gratings were written in two different fibers such that the LPFGs would exhibit two neighboring resonances showing well distinct responses to applied temperature and strain. One grating was induced in the Corning SMF-28 fiber by using the following fabrication parameters [6]:  $T = 22.8$  g,  $I = 9$  mA,  $t = 1$  s,  $540$   $\mu$ m,  $N = 40$ ; and the other in the Fibercore B/Ge codoped fiber ( $T = 22.8$  g,  $I = 8.5$  mA,  $t = 0.5$  s,  $415$   $\mu$ m,  $N = 42$ ). Second, the region in between the concatenated gratings was recoated to avoid recoupling by the second grating and also to extend the operating temperature range. The spectra of the two concatenated gratings are shown in Figure 1(a). The resonance ( $LP_{07}$ ) at shorter wavelengths belongs to the symmetric grating written in the Fibercore fiber and the resonance ( $LP_{14}$ ) at longer wavelengths results from the asymmetric grating arc-induced in SMF-28 fiber [7].

The sensor was calibrated, using the setup shown in Figure 1(b), by measuring its response to applied strain in the range 0–2000  $\mu$  $\epsilon$  and temperature in the range 35–100°C. Strain increased in steps of 200  $\mu$  $\epsilon$  at a constant temperature, and temperature was changed in steps of 5°C keeping the strain constant. At

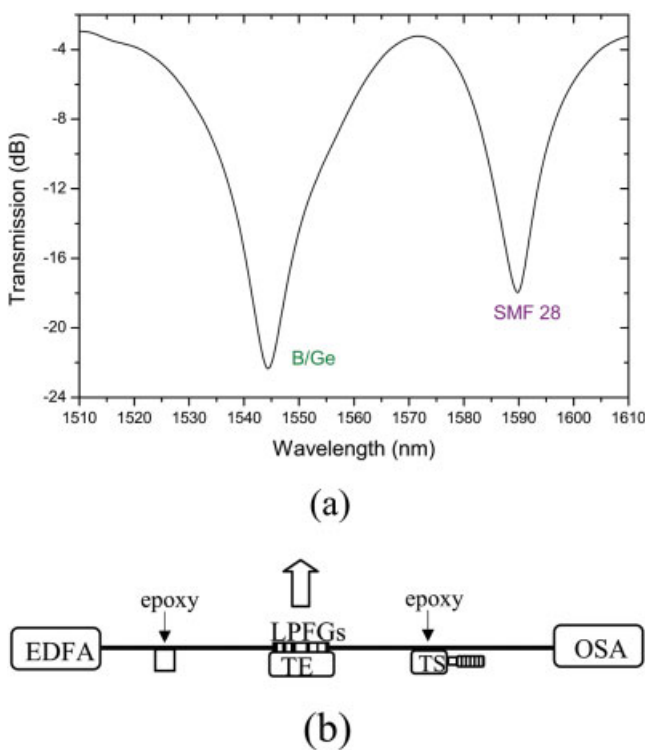


**Figure 1** Gratings transmission spectra and experimental setup. (a) Close-up of the two resonances under measurement. (b) Experimental setup for characterization of the sensing head. TEC: thermoelectric cooler; TS: translation stage. [Color figure can be viewed in the online issue, which is available at [www.interscience.wiley.com](http://www.interscience.wiley.com)]

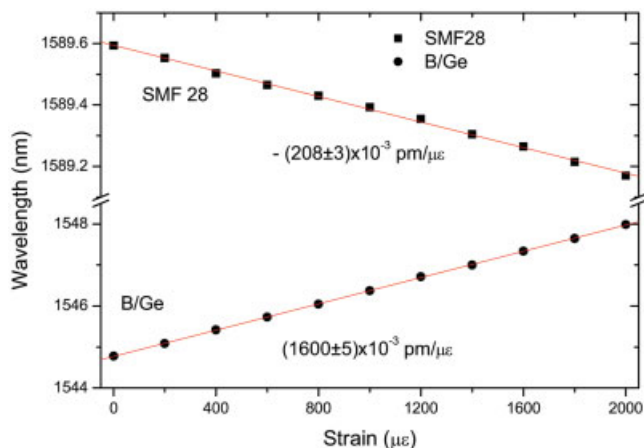


**Figure 2** Strain response of the sensing head (at constant temperature). [Color figure can be viewed in the online issue, which is available at [www.interscience.wiley.com](http://www.interscience.wiley.com)]

each step, the transmission spectrum of the grating was recorded using an optical spectrum analyzer. The results of calibration are presented in Figures 3 and 4. Figure 3 shows the strain dependence of the wavelengths of the two resonances. As we stretch the sensor the resonance belonging to the grating induced in the B/Ge codoped fiber shifts towards longer wavelengths whilst the other resonance shifts in the opposite direction. Both resonances show a linear dependence on strain being the sensitivity of the resonance belonging to the SMF-28 fiber one eighth of the other. The dependence of the resonance wavelengths on temperature is shown in Figure 4. As the temperature increases, the resonances shift in opposite directions, but this time they are moving towards each other since the shift of the resonances was reversed when compared to the effect of strain. Again, the dependence is linear being the temperature sensitivity eight times larger for the grating written in the B/Ge codoped fiber.

The slopes of the linear fittings are used in the matrix Eq. (1) that can be written as

$$\begin{bmatrix} \Delta T \\ \Delta \epsilon \end{bmatrix} = -83.7 \times 10^{-3} \begin{bmatrix} -0.208 & -1.6 \\ -62.2 & -421.0 \end{bmatrix} \begin{bmatrix} \Delta \lambda_1 \\ \Delta \lambda_2 \end{bmatrix} \quad (1)$$

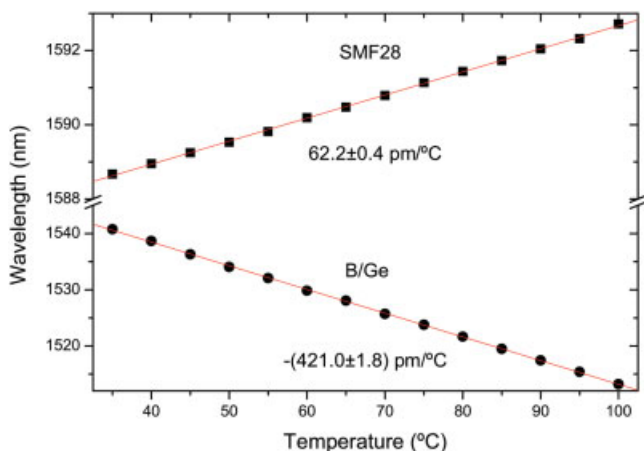


**Figure 3** Temperature response of the sensing head (constant strain). [Color figure can be viewed in the online issue, which is available at [www.interscience.wiley.com](http://www.interscience.wiley.com)]

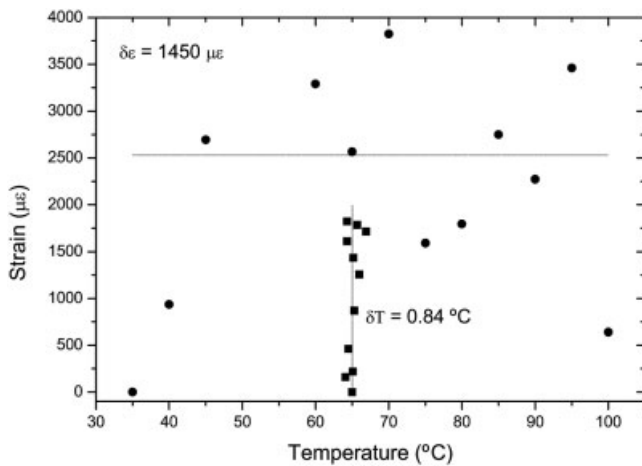


Figure 4 Sensor output as determined by Eq. (1)

where  $\Delta\lambda_1$  and  $\Delta\lambda_2$  are expressed in pm,  $\Delta T$  in  $^{\circ}\text{C}$  and  $De$  in  $\mu\epsilon$ .

The system resolution was estimated directly from the calibration procedure. As seen in Figure 4 this sensor is not suitable for the simultaneous measurement of temperature and strain [8, 9]. Although the error in the determination of the matrix coefficients is within 1.5%, the error in the calculation of the matrix determinant is quite high, above 20%. It is interesting to compare this result with the one obtained in Ref. 5. Both sensors have a similar determinant value of about 10, the error in the matrix coefficients was in that case twice larger and the uncertainty in the determinant was three times lower. Therefore, one may conclude that is the large difference in the gratings sensitivities that prevents the use of this sensor.

### 3. CONCLUSIONS

We described a sensor head consisting on the concatenation of two arc-induced LPPGs to be used in the simultaneous measurement of temperature and strain. It was demonstrated that due to the large difference in the temperature and strain sensitivities of the two gratings this sensor cannot reach the initial aim, since that leads to uncertainty in finding the determinant of the inverse matrix. Therefore, the choice of two gratings with completely different sensitivities to the parameters to be measured may not be the best option to implement a sensor.

### REFERENCES

1. V. Bhatia, D. Campbell, R.O. Claus, and A.M. Vengsarkar, Simultaneous strain and temperature measurement with long-period gratings, *Opt Lett* 22 (1997), 648–650.
2. G. Rego, R. Falate, O. Ivanov, and J.L. Santos, Simultaneous temperature and strain measurements performed by a step-changed arc-induced long-period fiber grating, *Appl Opt* 46 (2007), 1392–1396.
3. K.J. Han, Y.W. Lee, J. Kwon, S. Roh, J. Jung, and B. Lee, Simultaneous measurement of strain and temperature incorporating a long-period fiber grating inscribed on a polarization-maintaining fiber, *IEEE Photon Technol Lett* 16 (2004), 2114–2116.
4. Y.-G. Han, S. Lee, C.-S. Kim, J. Kang, U.-C. Paek, and Y. Chung, Simultaneous measurement of temperature and strain using dual long-period fiber gratings with controlled temperature and strain sensitivities, *Opt Express* 11 (2003), 476–481.
5. G. Rego, P.S. Marques, H.M. Salgado, and J.L. Santos, Simultaneous measurement of temperature and strain based on arc-induced long period fibre gratings, *Electron Lett* 41 (2005), 60–62.
6. G. Rego, P.S. Marques, H.M. Salgado, and J.L. Santos, Arc-induced long-period fiber gratings, *Fiber Integr Opt* 24 (2005), 245–259.
7. G. Rego, O. Ivanov, and P.V.S. Marques, Demonstration of coupling to

symmetric and antisymmetric cladding modes in arc-induced long-period fiber gratings, *Opt Express* 14 (2006), 9594–9599.

8. W. Jin, W.C. Michie, G. Thursby, M. Konstantaki, and B. Culshaw, Geometric representation of errors in measurements of strain and temperature, *Opt Eng* 36 (1997), 2272–2278.
9. W. Jin, W.C. Michie, G. Thursby, M. Konstantaki, and B. Culshaw, Simultaneous measurement of strain and temperature: Error analysis, *Opt Eng* 36 (1997), 598–609.

© 2008 Wiley Periodicals, Inc.

## ACCURATE INTEGRATION OF SEGMENTED 3D PROFILE MEASUREMENTS USING DIGITAL 2D FRINGE PROJECTION

Wei-Hung Su,<sup>1</sup> Yi-Ling Hsu,<sup>2</sup> Kun-Chang Yu,<sup>3</sup> and Hongyu Liu<sup>3</sup>

<sup>1</sup> Department of Materials Science and Optoelectronic Engineering, National Sun Yat-Sen University, Kaohsiung 804, Taiwan

<sup>2</sup> Institute of Material Science, National Sun Yat-Sen University, Kaohsiung 804, Taiwan

<sup>3</sup> Department of Electrical Engineering, The Pennsylvania State University, University Park, PA 16802; Corresponding author: wxs156@mail.nsysu.edu.tw

Received 11 January 2008

**ABSTRACT:** An improved integration approach for segmented 3D shapes using projected digitalized 2D pattern is presented. The digital 2D patterns are fabricated based on lithography techniques. Geometrical accuracy better than  $0.5 \mu\text{m}$  can be achieved. Contrast ratio of the fringe pattern can be precisely controlled as well. With this pattern, integrated accuracy better than one part in one hundredth of the pixel size can be achieved. © 2008 Wiley Periodicals, Inc. *Microwave Opt Technol Lett* 50: 2474–2480, 2008; Published online in Wiley InterScience (www.interscience.wiley.com). DOI 10.1002/mop.23667

**Key words:** fringe projection; 3D profile measurement; two-dimensional sinusoidal fringes; image registration; 3D data fusion

**PACS:** 42.30.-d, 42.30.Rx, 42.30.Sy, 42.30.Tz, 42.30.Wb

### 1. INTRODUCTION

The 3D-shape measurements using fringe projection methods has been extensively studied for automated manufacturing, component quality control, reverse engineering, and 3D animation [1–4]. It uses a fringe pattern projected on the inspected object and utilizes an image sensor array to observe the fringe distribution at a different viewpoint. Phase of the fringes deformed by the inspected shape is then used to retrieve the depth information. However, not many inspected objects are simple enough to be described by one full-field measurement. When the surface size is larger than the field of view of the measurement system or shadowing and occultation exists on the inspected surface, more segmented measurements from different viewpoints are required to form an entire shape.

The entire shape should be segmented in such a way that different regions overlap with each other. The overlapped regions provide useful information for addressing the changes in the orientation of the inspection system. The task of addressing points in the overlapped regions from the associated datasets is called image registration. Many algorithms have developed several methods to identify the matched datasets [5–9]. However, these techniques may not be directly applied to precision metrology due to the following limitations: (1) the algorithms based on the image intensity are very sensitive to surface reflectivity and image noise. (2) The algorithms based on the